Polymer Bulletin (2024) 81:6513–6537
https://doi.org/10.1007/s00289-023-05016-9

ORIGINAL PAPER

Efficient single-crystal 4-*N*,*N*-dimethylamino-4-*N*-methyl-stilbazolium tosylate (DAST) on the optical, piezoelectric coefficient and structure of P(VDF-HFP) copolymer for energy conversion systems

A. Habib[1] · **M. M. Metwally**[2] · **T. Fahmy**[1]

Received: 23 May 2023 / Revised: 17 September 2023 / Accepted: 23 September 2023 /
Published online: 16 October 2023

Abstract

Poly(vinylidene fluoride-co-hexafluoropropylene) P(VDF-HFP) doped with 4-*N*,*N*-dimethylamino-4-*N*-methyl-stilbazolium tosylate (DAST) composites with various concentrations of DAST dye is prepared using the casting method. The crystal structure and optical properties of the pure and P(VDF-HFP)/DAST composites with various contents of DAST dye are investigated using various techniques such as UV–Vis spectroscopy, X-ray diffraction (XRD), Fourier-transform infrared spectroscopy (FTIR) and polarized optical microscopy (POM). The analysis of XRD data and FTIR spectra revealed that the β-fraction has been improved in the composite samples with increasing the content of DAST dye. Analysis of UV spectra displayed that the optical band gap of P(VDF-HFP) pure copolymer is 5.41 eV and has been reduced to be 3.75 eV for P(VDF-HFP)/10 wt% DAST that will be suitable for efficient systems of energy conversion and multijunction-based layer solar cells. Also, it is found that the nonlinear and linear optical parameters of the composite samples are DAST dye-dependent. Thermally stimulated depolarization current (TSDC) technique has been applied to investigate the dipolar and space charge relaxations of the composites. Moreover, it is observed that the pyroelectricity and piezoelectricity are enhanced with increasing the content of DAST dye. The highest content of the DAST dye showed maximum values of the pyroelectric and the piezoelectric coefficients of ~ 4×10^{-5} C/m^2 K and ~ 34 pC/N at stress of 6.27×10^5 Pa, respectively. Our results of the polymer/dye composites give an opportunity of a promising material for flexible piezoelectricity devices used in many potential applications and energy harvesting systems.

Extended author information available on the last page of the article

Introduction

Energy harvesting converts the energy in the environment such as thermal energy, kinetic energy and light into electrical energy. Currently, the energy harvesting devices based on the piezoelectric materials have attracted more and more widespread attention [1]. Piezoelectric materials are classified into two different types: inorganic and organic materials. Materials such as lead zirconium titanate (PZT) and barium titanate $BaTiO_3$ (BTO), although they have relatively high piezoelectricity, are brittle and contain hazardous elements such as lead, which reduces their use in applications. On the other hand, the polymeric materials are light in weight and possess good formability, which qualifies them for effective energy harvesting applications. Poly(vinylidene fluoride) (PVDF) and its copolymers have attracted intense interest in several fields including microrobots, wireless sensor networks, microelectromechanical system operation and implantable biological devices due to their excellent flexibility and simple fabrication process [2, 3].

PVDF is one of the high molecular weight flexible hydrofluoropolymers that exhibit outstanding dielectric, pyroelectric and piezoelectric properties. Additional improvement of pyroelectricity and piezoelectricity can be recognized when the hexafluoropropylene (HFP) monomer units are combined with PVDF main matrix. Hence, the copolymer of P(VDF-HFP) with unique horizons can be obtained with crystal structures similar to those of PVDF with high chemical resistance and flexibility. Due to properties such as size, shape, recyclability, high stability and non-toxicity, these copolymers are widely gaining momentum in the technologies of energy harvesting [4, 5].

The P(VDF-HFP) copolymer has distinguished five phases such as, α, β, γ, δ and ε. α-Phase is a non-polar polymorph and is characterized by TGTG/polymeric chain conformation. However, the β-phase, which has a zigzag conformation (TTTT), is believed to be superior among the phases because of the largest dipole moment (8×10^{-30} Cm) compared to the polar phases, γ and δ phases [6]. Increasing the content of β-phase is one of the main factors for obtaining high piezoelectric materials. In recent years, the transition from α phase to β phase is a research topic that pays a lot of attention. A number of different methods have been widely used to prepare P(VDF-HFP) copolymer with large β-phase content such as high electric field [7], high pressure [8], uniaxial stretching [9, 10], annealing [11] and doping with different materials [12]. So, copolymer of P(VDF-HFP) with higher content of β-phase has currently received considerable attention for its outstanding performance in the in pyroelectric, piezoelectric and ferroelectric extents.

The crystal ionic organic salt DAST is extensively investigated as a nonlinear organic material because of its electro-optical material with large value and nonlinear optical (NLO) responses [13].

The improvement of organic materials with superior nonlinear optical (NLO) properties is a very active and vibrant area of research for use in a variety of promising applications such as switched lasers, optical reduction, bioimaging,

phototherapeutics, micro-fabrication and 3D optical data storage [14]. Recently, new applications of DAST have attracted significant interest in terahertz (THz) generations and detection [15].

In this study, we introduce the DAST dye to the copolymer P(VDF–HFP) matrix to prepare P(VDF–HFP)/DAST composites by solution casting method to nucleate the β-crystalline phase and eventually enhancing the pyroelectric and piezoelectric activities of the resulting composites. The influence of DAST dye on the phase transformation and optical behavior of P(VDF–HFP)/DAST composites is achieved using XRD, FTIR spectroscopy, UV–Vis spectroscopy and polarized optical microscopy (POM). Also, the relaxation behavior, pyroelectricity and piezoelectricity of the P(VDF–HFP)/DAST composites have been investigated intensively.

Experimental work

Materials

Organic crystal salt 4-*N*,*N*-dimethylamino-4′-*N*′-methyl-stilbazolium tosylate (DAST) with 99% pureness was supplied by Fluka. P(VDF-HFP) (10 wt% HFP; molecular weight of 400,000 g/mol; Solef 21,216) was obtained from Solvay (Brussels, Belgium). DMF (dimethylformamide with purity 99%) was obtained from Merck.

Sample preparation

Copolymer P(VDF-HFP) and DAST dye at different concentrations were dissolved separately in dimethylformamide (DMF) at room temperature and then mixed with each other with continuous stirring to obtain a homogeneous solution. Before pouring the solution, glass slides were washed and cleaned thoroughly with distilled water and then oven-dried for 15 min at 353 K to remove any residual moisture. Solutions of P(VDF-HFP)/DAST composites were poured onto glass slides and dried at 343 K for 2 h in an oven, to ensure that the remaining DMF solvent was evaporated. The sample thickness was measured with a digital micrometer (no. 292-521-30, Mitutoyo, Japan) and found to be ranged from 20 to 35 µm. The expected interaction between P(VDF-HFP) and DAST dye is explained in Scheme 1.

The presence of quaternary ammonium salt 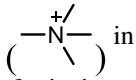 in the chemical structure of the DAST dye causes two possibilities to occur for its interaction with the fluorinated copolymer P(VDF-HFP) as shown in Scheme 1. The first expected mechanism can be illustrated by 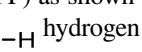 hydrogen bonding with the highest electronegative fluorine atoms [16]. However, two systems of a weak H-bond may be formed between sp^3 CH host or donor and sp^2 CH groups guest or acceptor, such as in C–H/π H-bond and C–H/ conjugated benzene rings in polymer and dye, respectively. The high withdrawing effect of the octafluoro atoms in P(VDF-HFP) polymer qualifies the tetrahedral sp^3 CH

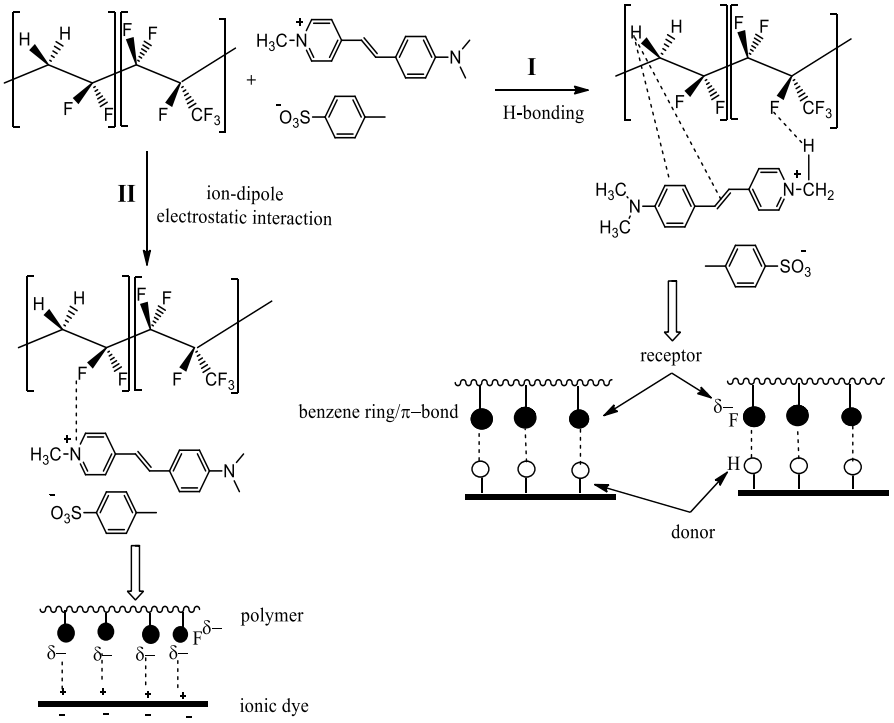

Scheme 1 The expected mechanisms of the interaction between P(VDF-HFP) and the ionic DAST dye

to be a strong guest for H-bond complex formation [17]. On the other hand, the ion–dipole interaction can be considered as the second pathway, as a result of the electrostatic interaction between the cationic quaternary ammonium part and the negatively partial charged fluorine atoms [18].

Methods and techniques

The crystalline structure was exanimated using X-ray diffraction (XRD Ultima II, Rigaku, Japan, electron probe current 40 mA and accelerating voltage 40 kV) in the range of 3°–65° with a resolution of 0.02° for all prepared samples. Measurements of FTIR (Fourier transformation infrared) were achieved using a Vertex 70, Bruker Optics (Germany) in an ATR mode at normal temperature of 4000–500 cm^{-1}. UV–Vis measurements of all samples were recorded using a Jasco V-570 spectrometer in the range from 190 to 1100 nm with a resolution of 5 nm. The optical polarized microscope (POM) (Jiangnan Novel, PM6000, China) was used to examine the surface morphology of the samples.

TSDC and pyroelectricity measurements

A homemade cell was used to perform the measurements of TSDC for all samples [19]. The samples were polarized in an oven at $T_p = 343$ K for polarizing time $t_p = 15$ min with various polarizing electric fields, E_p. Then, the samples were cooled down slowly to room temperature in the applied field to freeze the polarized dipoles. After removing the applied electric field, the samples were short-circuited for 15 min to remove any stray charges. The samples were reheated again with a linear heating rate of 3 K/min, and the depolarized current $I(T)$ was recorded through a Keithley 485 picometer. Measurements of the pyroelectricity were taken by cooling the sample again to room temperature after recording TSDC (first cycle) and then starting to heat the sample again at the same heating rate to record the resulting current (second cycle).

Piezoelectric measurements

For the piezoelectric measurements, the samples were polarized by applying constant electric field in the order of $E_p = 1.1 \times 10^7$ V/m at polarizing temperature $T_p = 363$ K for polarizing time of $t_p = 30$ min. The piezoelectric current was measured for our samples at various measuring temperatures (T_m) and different applying values of stress. The piezoelectric current was recorded by a Keithley 485 picometer, and then, the piezoelectric coefficient d_{33} was calculated.

Results and discussion

XRD

XRD pattern helps to provide the effect of DAST dye on the crystalline phases of PVDF-HFP copolymer, especially α and β phases. Figure 1 displays XRD pattern

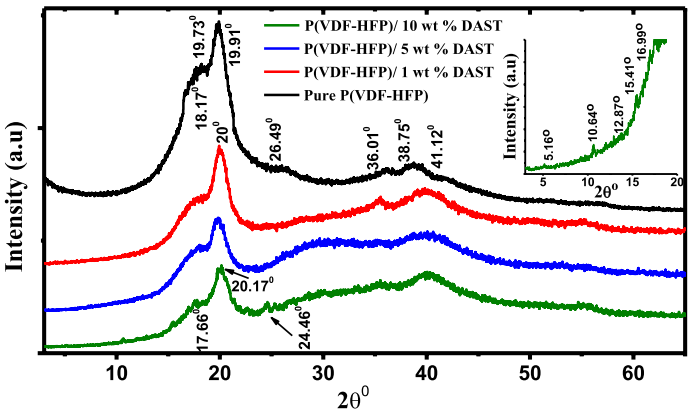

Fig. 1 XRD of pure P(VDF-HFP) and P(VDF-HFP)/DAST composite samples

of P(VDF-HFP) and P(VDF-HFP)/DAST composite samples. The peaks at 18.17°, 19.73°, 26.49°, 36.01° and 38.75° reveal the semicrystalline nature of PVDF-HFP copolymer. The diffraction peaks at 18.17°, 19.73° and 26.49° correspond to (020), (110) and (021) planes of the monoclinic α-phase [19]. The strong diffraction peak and weak peak at 19.91° and 36.01° correspond to (110)/(200) and (020) planes of the orthorhombic β-phase, which confirms the existence of the ferroelectric β-phase [20].

With increasing the content of DAST dye in the composite samples, some of the characteristic peaks of α-phase such as 18.17° and 26.49° almost disappeared and the intensity of the peak at 19.73° decreased. Also, the diffraction peak at 36.01° in pure P(VDF-HFP) is shifted toward a lower diffraction angle to appear at 35.49°, while the diffraction peak at 38.76° in pure PVDF-HFP is shifted to higher diffraction angle to appear at 40.07° in the highly doped composite sample. All these observations suggested that the polar phase of P(VDF-HFP) successively increased after doping with DAST dye. It means that β-phase fraction in the P(VDF-HFP)/DAST composite samples is improved, indicating that the P(VDF-HFP)/DAST composite may show a better piezoelectric response [21].

Different structural quantities such as crystallite size (D), lattice strain (ε_L), number of crystals per unit surface area (N_c) and dislocation density (δ) are important to obtain sufficient information about the structural transformation that occurred in the samples of the overlays. The values of crystallite size (D) and lattice strain (ε_L) are estimated by Debye–Scherrer formula as follows [22]:

$$D = \frac{0.9\,\lambda}{\beta \cos\theta} \tag{1a}$$

$$\varepsilon = \frac{\beta_{hkl}}{4\tan\theta} \tag{1b}$$

The number of crystallites per unit surface area (N_c) and dislocation density (δ) are estimated using the following expression [23]:

$$N_c = \frac{d}{D^3} \tag{2a}$$

Table 1 Structural parameters of pure P(VDF-HFP) and P(VDF-HFP)/DAST composites

Structural parameters	P(VDF-HFP)	P(VDF-HFP)/1 wt% DAST	P(VDF-HFP)/5 wt% DAST	P(VDF-HFP)/10 wt% DAST
D (nm)	7.94	7.00	5.99	5.76
ε	0.026	0.029	0.034	0.036
N_c (nm^{-2})	105.93	157.41	254.64	345.33
δ (nm^{-2})	0.015	0.020	0.027	0.030

$$\delta = \frac{1}{D^2} \tag{2b}$$

where d is the sample thickness. The calculated structural parameters of all samples are summarized in Table 1.

FTIR-Spectroscopy

Figure 2 displays FTIR spectra of P(VDF-HFP) and P(VDF-HFP)/DAST composites. The bands at 3012 cm^{-1} and 2970 cm^{-1} in the spectrum of P(VDF-HFP) copolymer are attributed to the asymmetric and symmetric stretching of CH_2 group, respectively [24]. The transmission band at 1402 cm^{-1} represents a combination between the three phases, i.e., α, β and γ [25, 26]. The bands at 1172 cm^{-1} and 1074 cm^{-1} are related to a combination of β and γ phases [25]. The band at 988 cm^{-1} is attributed to the non-electroactive α phase and assigned as C–F stretching vibration [27]. Moreover, FTIR of pure P(VDF-HFP) copolymer involving many transmission bands at 836 cm^{-1} is related to β-polar phase and assigned as (CF_2 stretching), 762 cm^{-1} (CF_2 bending), 615 cm^{-1} (skeletal bending), 511 cm^{-1}

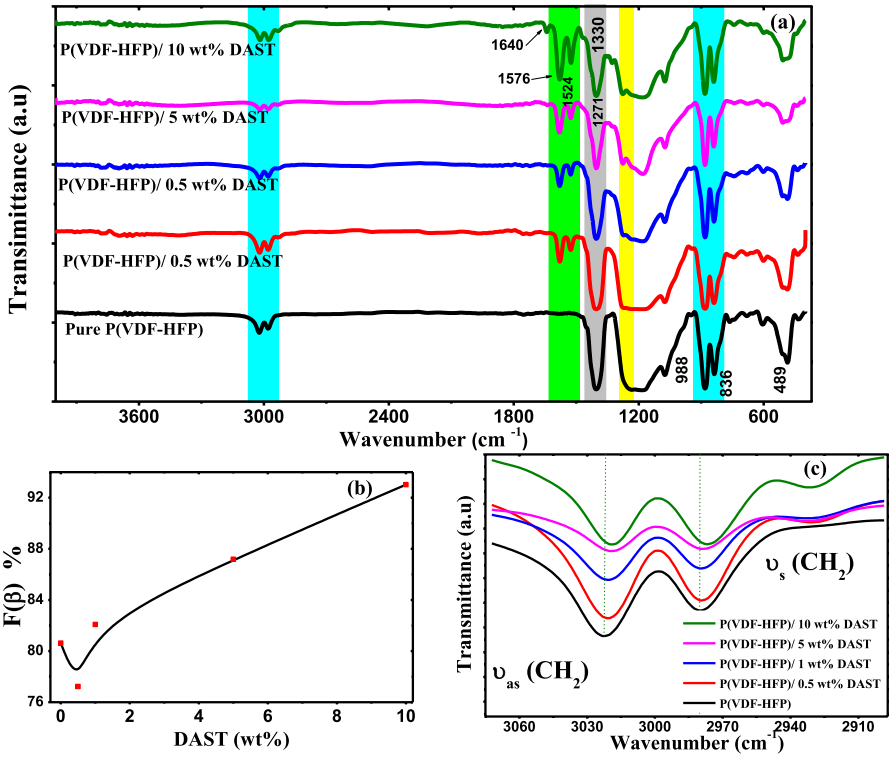

Fig. 2 **a** FTIR of P(VDF-HFP) and P(VDF-HFP)/DAST composites, **b** F (β) versus DAST content and **c** CH_2 bands in the region from 3080 cm^{-1} to 2900 cm^{-1} of pure and P(VDF-HFP)/DAST composite samples

(CF_2 stretching) and 489 cm^{-1} (CF_2 waging) [4, 28, 29]. The transmission bands at 1402 cm^{-1}, 950 cm^{-1}, 762 cm^{-1}, 606 cm^{-1} and 489 cm^{-1} are attributed to α-phase, while the bands at 836 cm^{-1} and 511 cm^{-1} correspond to β-phase, as shown in Fig. 2a [12, 30]. These results suggest both α and β-phases are formed by the VDF segments in the P(VDF-HFP) copolymer. On the other side, with increasing the DAST dye content, the α-phase bands become much weaker, while the intensity of β-phase bands increases, confirming that the addition of DAST dye can stimulate β-phase formation during the initial crystallization process, as shown in Fig. 2a. FTIR spectrum of DAST dye displayed many transmission bands at 1640 cm^{-1}, 1577 cm^{-1}, 1524 cm^{-1}, 1271 cm^{-1} and 1330 cm^{-1} [31]. The characteristic bands and their assignments of P(VDF-HFP)/DAST composites are listed in Table 2.

The relative β-phase fraction $F(\beta)$ in PVDF-HFP/DAST composites is estimated using the following formula [32]:

$$F(\beta) = \frac{A_\beta}{1.26A_\alpha + A_\beta} \tag{3}$$

where A_β and A_α are the absorbance at both 836 cm^{-1} and 762 cm^{-1}, respectively. It is found that the relative β-phase fraction is increased with increasing the DAST dye content in PVDF-HFP/DAST composites, indicating that DAST dye has a clear effect on the transformation of α phase to β-phase, as shown in Fig. 2b. The relative β-phase fraction became ~ 93.10% for P(VDF-HFP) after doping with 10 wt% of DAST dye. Hence, we can say that the nucleation of the electroactive β-phase is enhanced in P(VDF-HFP) copolymer after the doping with DAST dye. The gradual enhancement of β-polar phase after doping P(VDF-HFP) with DAST may be due to the interfacial electrostatic interaction between positively charged $–CH_2$ dipole

Table 2 The wavenumber and assignments of PVDF-HFP/DAST composite samples

Wavenumber (cm^{-1})	Assignment	References
3012	Asymmetric stretching of CH_2 group	[1]
2970	Symmetric stretching of CH_2 group	[1]
1640	Vibrational (C=C)/vinyl (C–H) rock	[9]
1577	Stretching vibrational (C=C)/vibrational (C–C)	[9]
1524	Ring Vibrational (C=C)	[9]
1271	Ring δ (C–H)	[9]
1330	Ring ν (C–C)	[9]
1402	A combination of the three phases α, β and γ	[2, 3]
1172	Assigned to a combination of β and γ phases	[2]
1074	Mostly the β phase	[2]
836	β-phase (the vibration of vinylidene group)	[4–6]
762	CF_2 bending	[4–6]
606	C–F wagging	[7, 8]
511	CF_2 stretching	[4–6]
489	CF_2 wagging	[4–6]

of P(VDF-HFP) copolymer and DAST dye [33]. This interaction will increase the zigzag conformation (TTTT) of the P(VDF-HFP) main chain which in turn will enhance the β-phase [34]. Thus, DAST dye acts as a β-phase-promoting nucleation agent. The gradual enhancement of interfacial interaction between CH_2 dipoles of P(VDF-HFP) and DAST dye can be confirmed by investigation their transmission FTIR bands in the region from 3080 to 2900 cm^{-1}, where the stretching vibrations of $–CH_2$ dipoles are responsible for the existence of these bands. The shift of the $–CH_2$ stretching vibration bands toward the lower energy region confirmed the gradual enhancement of the interfacial interaction in P(VDF-HFP)/DAST composite samples, as shown in Fig. 2c [24]. The interaction between the charges distributed on the DAST dye surface and $–CH_2$ dipoles acting as a damping source for the $–CH_2$ dipoles oscillation results in a shift of the vibrational bands toward a lower energy region (lower wavenumber). This behavior is interpreted using the damped harmonic oscillation of $–CH_2$ dipole [35].

Morphology

The spherulitic morphology of a P(VDF-HFP) and its composites could be observed using the polarized optical microscopy (POM). Figure 3 displays the optical micrographs of P(VDF-HFP) and P(VDF-HFP)/DAST composite samples with various concentrations of DAST dye. The morphology of P(VDF-HFP) copolymer displayed a spherulitic pattern. It was found that the P(VDF-HFP) copolymer had an unequal-grained rough surface with small dark pores with a laminar distribution confirming

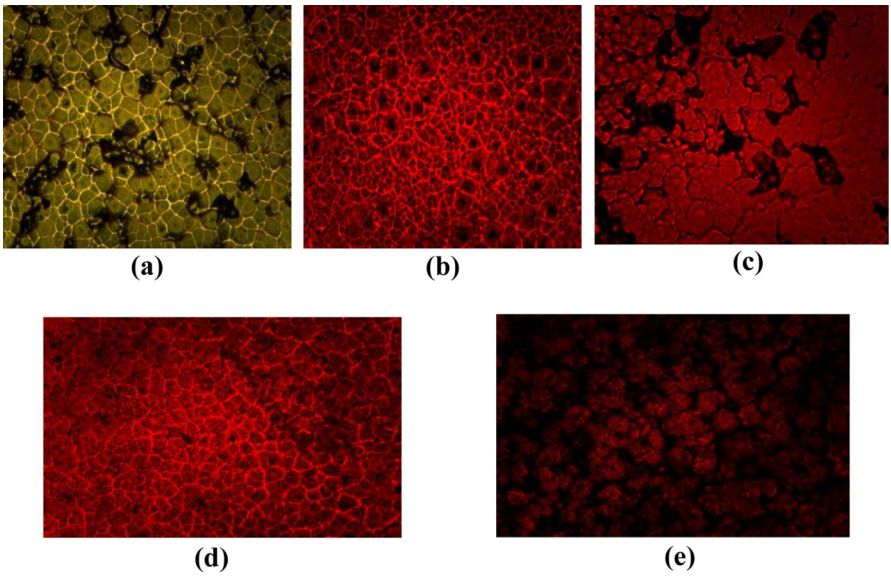

Fig. 3 Optical morphology of **a** P(VDF-HFP), **b** P(VDF-HFP)/0.5 wt% DAST, **c** P(VDF-HFP)/1 wt% DAST, **d** P(VDF-HFP)/5 wt% DAST, **e** P(VDF-HFP)/10 wt% DAST

the semicrystalline nature of P(VDF-HFP), as illustrated in Fig. 3a [36]. Evaporation of the solvent may lead to the formation of dark areas of the pores. The crystalline α-phase of P(VDF-HFP) copolymer is thus confirmed due to the presence of the spherulites [37, 38]. The P(VDF-HFP)/DAST composite samples showed that the DAST dye was uniformly distributed without agglomeration in the copolymer matrix and the porosity was also reduced, as illustrated in Fig. 3b–e. Also, it is observed that the dispersion of DAST dye becomes more uneven with increasing the DAST dye content, as shown in Fig. 3d, e. With increasing the DAST content increases, the spherulites interact with each other forming a larger spherulites.

UV–vis part

Figure 4a displays the optical absorption (A) of P(VDF-HFP) and P(VDF-HFP)/DAST composite samples. It can be seen that the absorption increases with increasing the content of DAST dye in composites because the dipoles number was increased, which indicates that a non-polar α-phase transformation into a β-polar phase has taken place [39]. The absorption spectrum of pure P(VDF-HFP) showed

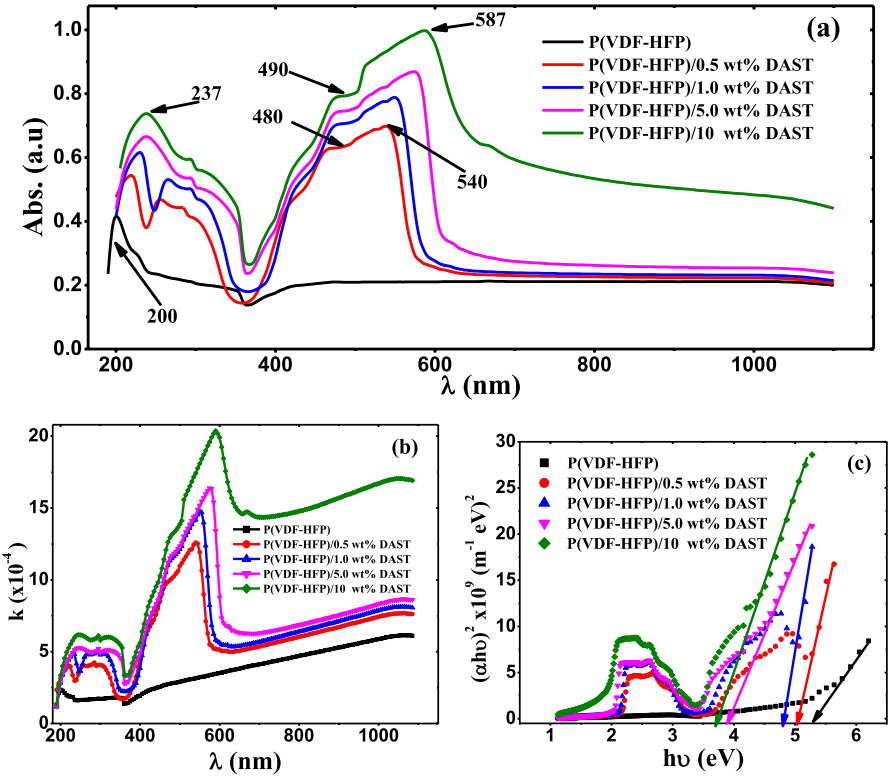

Fig. 4 **a** The absorption against wavelength, **b** the extinction coefficient (k) against wavelength and **c** $(\alpha h\nu)^2$ against $h\nu$

an absorption peak at 200 nm and is red shifted to appear at 237 nm in the highly doped composite sample. This shift is attributed to the strong electrostatic interaction between DAST dye and P(VDF-HFP) copolymer main chain. Also, the absorption spectra of P(VDF-HFP)/DAST composites showed a shoulder centered at 480 nm and a peak at 540 nm in the low doped samples and are red shifted to appear at a shoulder centered at 490 nm and a peak at 587 nm with increasing the DAST in the composite samples. The shoulder at 480 nm is due to the absorption of DAST molecules. The red shift in the absorption bands of DAST dye in the composite samples may be due to the J-aggregation of the chromophores as reported previously [13, 40]. The extinction coefficient (k) is estimated using the absorption coefficient α, as $k = \alpha\lambda/4\pi$, where $\alpha = 2.3\ A/t$, in which t is the thickness of the sample. The variation of the extinction coefficient against the wavelength is shown in Fig. 4b. It is observed that with increasing the DAST dye content in the composite samples k increases, indicating higher light dissipation due to absorption and scattering by DAST centers in agreement with the results of Mott and Davis [41]. The strong interaction between DAST and P(VDF-HFP) copolymer leads to a change in crystallinity and thus a change in the band structure and absorption ratio. In general, it is observed that the extinction coefficient (k) in the UV region decreases with increasing wavelength, while in the visible region (400–1100 nm) it starts to increase again with increasing wavelength. In the UV region, the incident photons have a suitable energy that enables them to excite the electrons for overcoming the band gap, and thus, the extinction coefficient values will decrease. Low values of k in this region indicate that electromagnetic waves can pass through P(VDF-HFP)/DAST composites without any damping. On the other hand, the photon energy does not enable it to excite the electrons from one state to another in the visible light region, so this energy due to scattering or reflection will be lost, which causes the k values in the visible region to increase again [42–44].

The optical band gap (E_g) of pure and P(VDF-HFP)/DAST composite samples is calculated based on Tauc's equation as follows:

$$\alpha h\upsilon = B\left(h\upsilon - E_g\right)^y \tag{4}$$

where hν is the incident photon energy and B is a constant, depending on the probability of the transition in the optical wavelength region. The index y gives valuable information about the electronic transition nature within the materials. For the direct and indirect allowed transitions, the index y will be ½ and 2, whereas for the direct and indirect forbidden transitions it will be 3/2 and 3, respectively. In the present work, the allowed direct transition is considered to estimate the optical band gap (E_g) for our samples, as shown in Fig. 4c.

By extrapolating the linear portion on the x-axis, i.e., $(\alpha h\nu)^2 = 0$, the optical band gap (E_g) is determined and listed in Table 3. It is observed the values of E_g are reduced with increasing the DAST content and changed from 5.41 eV for P(VDF-HFP) to 3.75 eV for P(VDF-HFP)/10 wt% DAST composite samples. This reduction may be due to the ability of DAST dye to enhance charge transfer between the DAST and P(VDF-HFP) matrix, leading to a dramatic change in the band structure of the composite samples [45].

Table 3 The optical parameters values of P(VDF-HFP)/DAST composite samples

	P(VDF-HFP)	P(VDF-HFP)/0.5 wt% DAST	P(VDF-HFP)/1 wt% DAST	P(VDF-HFP)/5 wt% DAST	P(VDF-HFP)/10 wt% DAST
Direct bandgap energy, (eV)	5.41	5.05	4.80	3.91	3.75
E_0, (eV)	6.34	4.44	3.69	3.70	3.48
E_d, (eV)	19.70	13.25	7.13	6.60	4.49
n_0	2.03	1.99	1.71	1.67	1.51
ε_s	4.11	3.98	2.93	2.78	2.29
ε_L	7.08	19.95	19.84	20.96	21.02
N/m*(m^{-3} kg^{-1})	1.71×10^{58}	8.54×10^{58}	8.80×10^{58}	9.73×10^{58}	1.02×10^{59}
ω_p (Hz)	7.04×10^{15}	1.59×10^{16}	1.60×10^{16}	1.68×10^{16}	1.71×10^{16}
$\chi^{(1)}$	0.247	0.237	0.154	0.142	0.103
$\chi^{(3)}$ (e.s.u.)	6.69×10^{-13}	5.71×10^{-13}	1.017×10^{-13}	7.31×10^{-14}	1.99×10^{-14}
n_2, (e.s.u)	1.47×10^{-12}	1.93×10^{-12}	2.37×10^{-12}	5.39×10^{-12}	6.37×10^{-12}

The dispersion model and optoelectronic parameters

The refractive index (n) dispersion is an important factor for designing highly efficient optical devices [46]. Dispersion parameters such as dispersion energy (E_d), effective oscillator energy (E_0), static refractive index (n_0) and static dielectric constant (ε_s) can be estimated by applying the single oscillator (SOM) model below the interband absorption edge using the following equation [47]:

$$n^2 = 1 + \frac{E_0 E_d}{E_0^2 - (h\upsilon)^2} \tag{5}$$

$$\left(n^2 - 1\right)^{-1} = \frac{E_0}{E_d} - \frac{1}{E_0 E_d}(h\upsilon)^2 \tag{6}$$

Figure 5a illustrates the dependence of $(n^2-1)^{-1}$ on $(h\nu)^2$ for all samples. The values of E_d and E_0 are determined by knowing the values of intercept (E_0/E_d) and slope ($1/E_0E_d$) of Fig. 5a and given in Table 3. It is noted that as the DAST content increases in the composite samples, both E_0 and E_d decrease. The decrease in the values of E_0 and E_0 can be attributed to the microstructure change in P(VDF-HFP) after doping with DAST dye. The values of E_0 and E_0 are employed to estimate the static refractive index (n_0) and static dielectric constant (ε_0) at zero frequency using the following equation:

$$\varepsilon_0 = n_0^2 = 1 + \frac{E_d}{E_0} \tag{7}$$

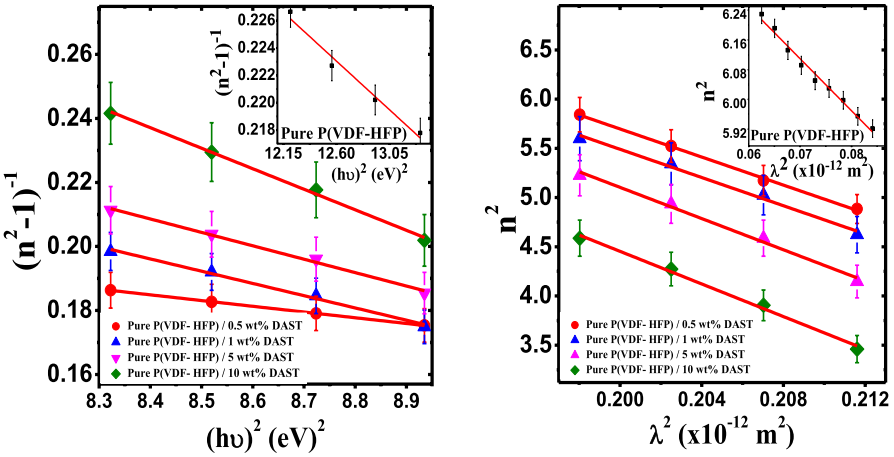

Fig. 5 **a** $(n^2-1)^{-1}$ versus $(h\nu)^2$ **b** n^2 versus λ^2

The values of n_0 and ε_s for pure and P(VDF-HFP)/DAST composites are calculated and given in Table 3. It is noted that both n_0 and ε_s values are decreased with DAST dye content increase in the composite samples. The relation between the square of refractive index (n^2) and wavelength (λ^2) can be expressed as follows:

$$n^2 = \varepsilon_L - \frac{1}{4\pi\varepsilon_0}\left(\frac{e^2}{c^2}\right)\left(\frac{N}{m^*}\right)\lambda^2 \tag{8}$$

where ε_L is the lattice dielectric constant at high frequency, $\varepsilon_0 = 8.85\times10^{-12}$ Fm^{-1}, $c = 3\times10^8$ m/s, $e = 1.6\times10^{-19}$ C, N is the carrier charge concentration and m^* is the effective mass of the carrier. The plot of n^2 against λ^2 yields straight lines with intercept of ε_L and slope of $\frac{1}{4\pi\varepsilon_0}\left(\frac{e^2}{c^2}\right)\left(\frac{N}{m^*}\right)$, as illustrated in Fig. 5b. The values of ε_L and (N/m^*) are estimated and given in Table 3. The results revealed that the values of lattice dielectric constant (ε_L) are higher than the values of static dielectric constant (ε_s). The variation between values of ε_L and ε_s can be attributed to the increase of free carriers concentration and the polarization process that arises in the material when it is exposed to light [43, 48]. The plasma frequency values of P(VDF-HFP)/DAST composite samples are determined and listed in Table 3 based on the following equation:

$$\omega_p = \sqrt{\left(\frac{e^2}{\varepsilon_0}\right)\left(\frac{N}{m^*}\right)} \tag{9}$$

It is found that the plasma frequency depends on the DAST content, that is, it increases with increasing the DAST content. This behavior is attributed to the high values of charge carrier concentration.

The simple empirical equations according to the generalized Miller's rule are used to calculate the linear and nonlinear optical parameters of P(VDF-HFP)/DAST

composites such as the first ($\chi^{(1)}$) and third ($\chi^{(3)}$) order of the optical susceptibility and nonlinear refractive index (n_2). These parameters are estimated by combining Miller's generalized rule and the relations concerning ($\chi^{(1)}$) and ($\chi^{(3)}$) containing the parameters of (SOM) model as follows [49]:

$$\chi^{(1)} = \frac{E_{\mathrm{d}}}{4\pi E_0} \tag{10}$$

$$\chi^{(3)} = 1.79 \times 10^{-10} \left(\chi^{(1)}\right)^4 \tag{11}$$

$$n_2 = \frac{12\,\pi\,\chi^{(3)}}{n_0} \tag{12}$$

The values of $\chi^{(1)}$, $\chi^{(3)}$ and n_2 are estimated and given in Table 3. It was found that as the DAST content in the composite samples increased, the value of these parameters increased.

TSDC

TSDC technique has proven to be a powerful method for understanding the defect properties both quantitatively and qualitatively. It has been applied to polymers and polymer composites to interpret the different relaxation mechanisms for decades [50–56]. Figure 6a displays TSDC global spectrum of pure P(VDF-HFP) samples in the temperature range from 300 to 395 K polarized under various electric fields. It is found that TSDC spectrum of P(VDF-HFP) is characterized by two intense relaxation peaks. The first peak is detected in the temperature range of 327–335 K, while the second peak is detected at about 375 K. Generally, the maximum current (I_{m}) of each relaxation peak is found to be field dependent, and it increases with increasing the applied electric field (E_P), as illustrated in the inset of Fig. 6a. It is well known that P(VDF-HFP) is a polar semicrystalline copolymer. The contribution of P(VDF-HFP) to the polarization process may be attributed to the dipole's orientation and the formation of space charge/charge carrier injection from the metallic electrode at high temperatures under applying the electric field. The first peak which is observed in the range 327–335 K can be assigned as α-relaxation. The α-relaxation in P(VDF-HFP) is referred as a dipole relaxation process that arises as a result of the localized rotational fluctuations of the dipoles [57]. The α-relaxation in P(VDF-HFP) can be related to the dipole's orientation of the polar side group (CH_2–CF_2). This relaxation peak has been reported for PVDF blends or composites of PVDF previously in the literature [58, 59]. The second relaxation peak at high temperature can be designated as ρ-peak which may arise from the charge carrier injection of from the metallic electrodes to the polymer surface, which is immobilized through the sample polarization process. P(VDF-HFP) may contain a large number of impurity molecules before the electric field treatment, and these molecules will separate into different ionic species. Hence, it is appropriate to attribute the relaxation peak that appear in

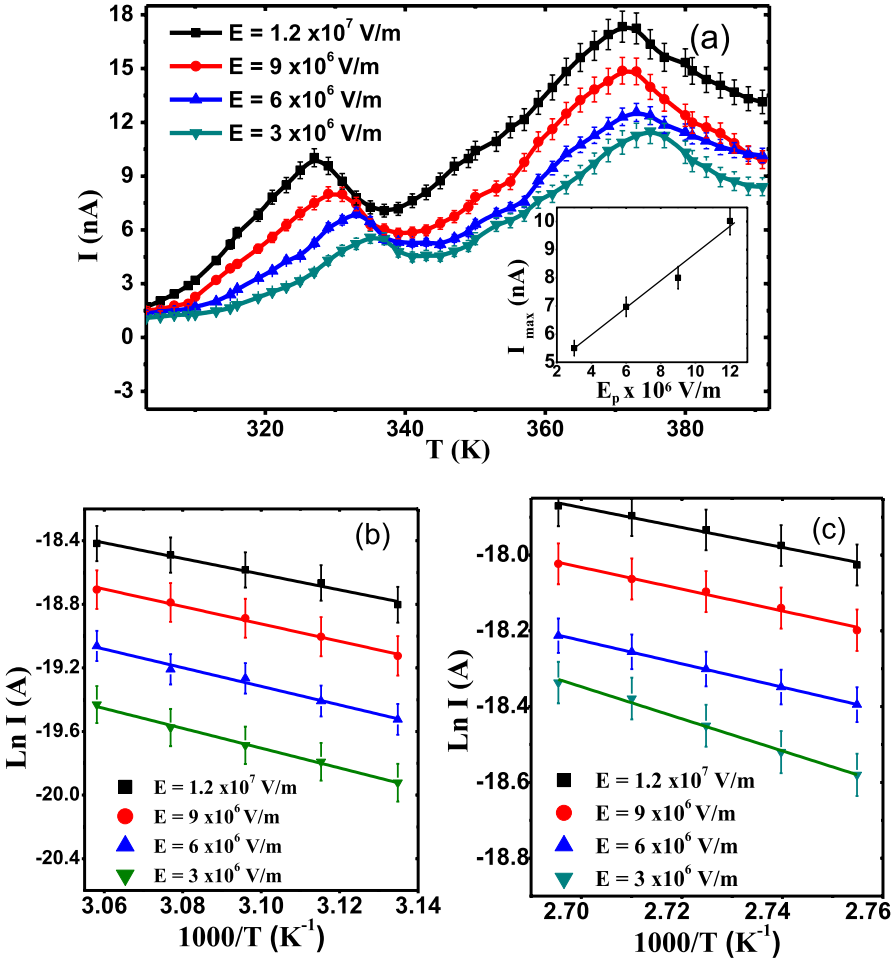

Fig. 6 **a** Global TSDC spectra of P(VDF-HFP) at various poling electric (E_p), $T_p = 343$K, $t_p = 15$ min. **b** Ln I against 1000/T for the first peak and **c** Ln I against 1000/T for the second peak

the high temperature range to the relaxation of space charge, which arises from the injection of charge carriers from the electrodes into the polymer–metal interface.

The depolarizing current of group of dipoles as a function of the temperature is expressed as follows [60, 61]:

$$I(T) = \frac{Q}{T} \exp\left(-\frac{E_a}{k_B T}\right) \exp\left[-\frac{1}{\beta \tau_0} \int_{T_0}^{T} \exp\left(-\frac{E_a}{k_B T'}\right) dT'\right] \tag{13}$$

where Q is the total charge released, E_a is the activation energy, β is the heating rate (dT/dt), k_B is the Boltzmann constant, T_o is the initial temperature at which the

depolarization current begins to appear and τ_o is a pre-exponential factor and is expressed as follows:

$$\tau(T) = \tau_0 \exp\left(\frac{E_a}{k_B T}\right) \tag{14}$$

where $\tau(T)$ is the relaxation time at a given temperature (T). Discharge current against the temperature to release the trapped charge carriers has the same form as Eq. 1. Hence, the shape of the thermal current spectrum generated by the traps as well as from dipoles is similar to each other. The low-temperature tail of Eq. 13 is expressed as follows:

$$\ln I(T) = \ln I_0 - \frac{E_a}{k_B T} \tag{15}$$

Hence, the activation energy (E_a) values of the depolarization process can be estimated using the slope of Eq. 15. When differentiating Eq. (13) with respect to temperature and equating the resulting equation to zero (i.e., $dI/dT = 0$), we can obtain the maximum temperature (T_m) at which the maximum current (I_m) will occur. The maximum temperature (T_m) is given by:

$$\tau_0 = \frac{k_B T_m^2}{\beta E_a} \exp\left(-\frac{E_a}{k_B T_m}\right) \tag{16}$$

The initial rise method has been applied based on Eqs. (15 and 16) to calculate all the molecular parameters of different relaxation processes of pure P(VDF-HFP) [62], as depicted in Fig. 6b, c and listed in Table 4.

The effect of DAST dye on TSDC spectrum of P(VDF-HFP) at constant poling temperature and poling electric field is illustrated in Fig. 7. It is found that as the content of DAST dye is increased, the current (I_m) of each relaxation peak of P(VDF-HFP)/DAST composite samples is increased in magnitude and also the temperature (T_m) of each relaxation peak is shifted to a higher temperature. The

Table 4 The molecular parameters of P(VDF-HFP) copolymer of the first and second peaks

E_p (V/m)	T_m (K)	E_a (eV)	τ_{o1} (s)	I_m (nA)
First peak				
3×10^6	335	0.53	2.92×10^{-6}	5.61
6×10^6	332	0.50	8.30×10^{-6}	6.82
9×10^6	329	0.47	2.30×10^{-5}	8.10
1.2×10^7	326	0.42	1.16×10^{-4}	9.90
Second Peak				
3×10^6	374	0.36	8.1×10^{-3}	1.15
6×10^6	372	0.26	0.23	1.26
9×10^6	372	0.24	0.43	1.47
1.2×10^7	371	0.22	0.87	1.75

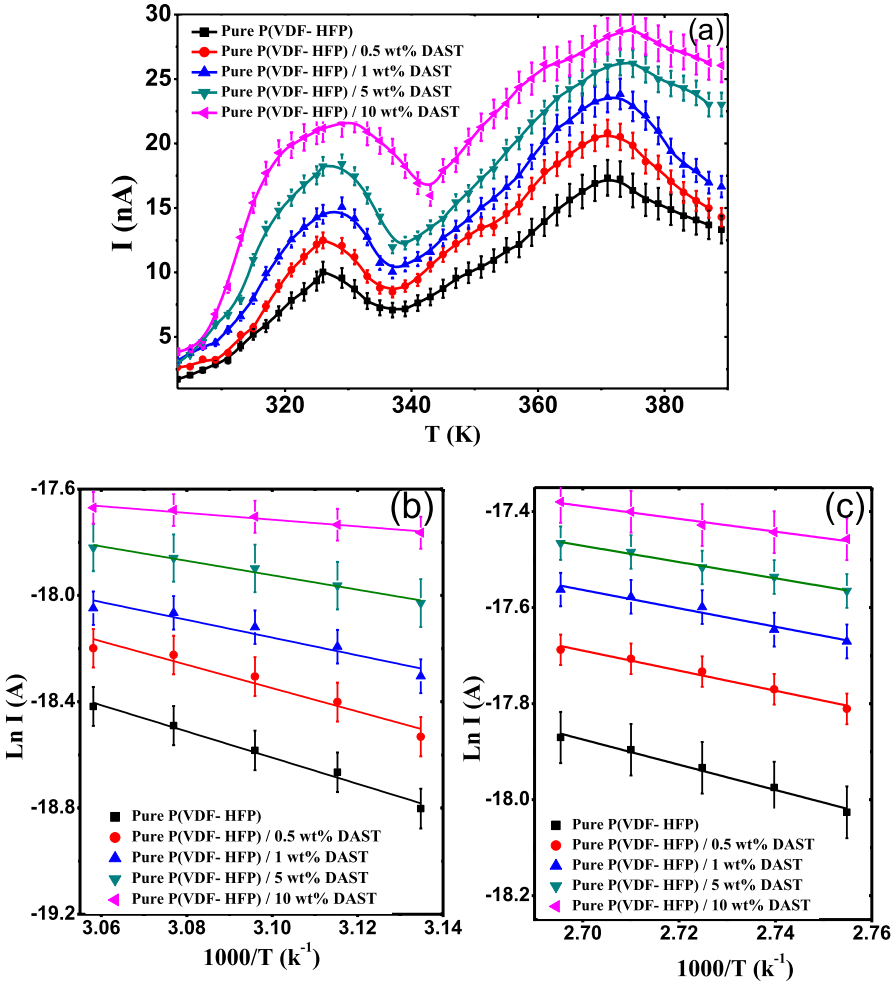

Fig. 7 **a** TSDC of P(VDF-HFP) and P(VDF-HFP)/DAST composites polarized with $E_p = 1.2 \times 10^7$ V/m, $t_p = 15$ min, $T_p = 343$K. **b** Ln I versus 1000/*T* for first peak and **c** Ln I versus 1000/*T* for second peak

activation energy (E_a) of each relaxation process of P(VDF-HFP)/DAST composite samples has been estimated using Eq. 15 as illustrated in Fig. 7b, c and given in Table 5. It is noted that the value of E_a for α-relaxation of pure P(VDF-HFP) is ranged from 0.42 to 0.53 eV, while that for P(VDF-HFP)/DAST composites is ranged from 0.11 to 0.42 eV. On the other hand, the value of E_a for ρ-relaxation of pure P(VDF-HFP) is ranged from 0.23 to 0.36 eV, while that for P(VDF-HFP)/DAST composites is ranged from 0.11 to 0.18 eV. The decrease in the values of E_a in the composite samples comparing to pure P(VDF-HFP) confirms the interaction between DAST dye and P(VDF-HFP) leading to an increase in the amorphous character of P(VDF-HFP). Our results are in good agreement with the reported data [58, 59].

Table 5 The molecular parameters of P(VDF-HFP) and P(VDF-HFP)/DAST composites of the first and second peaks

Sample	T_m (K)	E_a (eV)	τ_{o1} (s)	I_m (nA)
First peak				
P(VDF-HFP)	326	0.42	1.16×10^{-4}	9.9
P(VDF-HFP)/0.5 wt% DAST	326	0.38	6.64×10^{-4}	12.2
P(VDF-HFP)/1 wt% DAST	328	0.29	0.024	14.6
P(VDF-HFP)/5 wt% DAST	329	0.23	0.21	18.5
P(VDF-HFP)/10 wt% DAST	330	0.11	37.9	21.8
Second peak				
(PVDF-HFP)	371	0.23	0.87	17.5
P(VDF-HFP)/0.5 wt% DAST	371	0.18	4.70	20.8
P(VDF-HFP)/1 wt% DAST	372	0.16	8.80	23.9
P(VDF-HFP)/5 wt% DAST	372	0.15	17.4	26.6
P(VDF-HFP)/10 wt% DAST	374	0.11	60.02	28.6

Pyroelectricity

The effect of DAST dye on the pyroelectric coefficient of P(VDF-HFP) is investigated, and the pyroelectric current is recorded against the temperature with a heating rate of 3 K/min, as shown in Fig. 8. The measured pyroelectric current expresses the polarization that induced from thermal stress. The pyroelectric coefficient is expressed as follows:

$$I = PA\frac{dT}{dt} \tag{17}$$

where I, P and A are the pyroelectric current, pyroelectric coefficient and electrode area, respectively. It is noted that as the temperature of the samples increased as well as the content of DAST in the P(VDF-HFP)/DAST composites increased, the

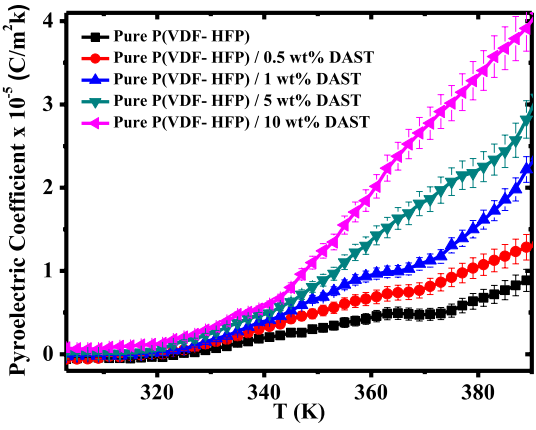

Fig. 8 The pyroelectric coefficient of P(VDF-HFP) and P(VDF-HFP)/DAST composites

pyroelectric coefficient value increased. Furthermore, the composite samples are found to be very sensitive in the temperature range of 337–395 K, where the pyroelectric coefficient changed from 0.69 to 4.12×10^{-5} C/m^2 K. This may be attributed to the structural relaxation process at low temperature due to the molecular motion in the crystalline region [63]. These results revealed that the embedding of DAST dye improved the pyroelectric properties of P(VDF-HFP) and thus modified the polarization behavior of the samples. In other words, it can be said that the incorporation of DAST dye into P(VDF-HFP) matrix enhances directly the β-phase of P(VDF-HFP) as verified from FTIR spectra, and β-phase causes the strong pyroelectric and piezoelectric response of P(VDF-HFP) [62]. The high pyroelectric activity of composite samples gives a real possible application as temperature sensor, especially in the temperature range 337–395 K [64].

Piezoelectricity activity

Figure 9 displays the variation of the piezoelectric coefficient (d_{33}) of P(VDF-HFP) and P(VDF-HFP)/DAST composite samples as a function of stress at different measuring temperatures. The samples are polarized at $T_p=363$ K with electric field of $E_p=1.2\times10^7$ V/m. Generally, it is found that the piezoelectric coefficient is temperature and stress dependent. During the poling process, a portion of α-phase may be transferred into β-phase and the dipoles of β-phase will align perpendicularly to the sample. The formation of β-phase in P(VDF-HFP) can be improved using various methods, such as polymer blending, poling under high electric field and the crystallization under high pressure [38, 65, 66]. The main function of the electric field is to unify the dipole directions of the β-phase, and thus, the piezoelectricity is expected to be improved more significantly at the higher field as shown in Fig. 9a [5, 67]. Also, it is found that the piezoelectric coefficient of P(VDF-HFP)/DAST composites has been enhanced with increasing the DAST ionic crystals content, as shown in Fig. 9b. The enhancement of piezoelectric coefficient of composite samples can be ascribed to relative extents of polar β-phase within the composites after doping with DAST, as confirmed from the analysis of X-ray data and FTIR spectra. In other words, the enhancement of β phase in P(VDF-HFP)/DAST composites and hence the piezoelectric coefficient could be ascribed to the interaction between the oppositely charged surface of DAST and the dipoles –CF_2–CH_2– of P(VDF-HFP). Also, improvement of the DAST crystals nucleation and surface charge polarization can produce more stable piezoelectric β-crystal phase [68]. The piezoelectric coefficient of highly doped composite sample, P(VDF-HFP)/10 wt% DAST, is investigated as a function of stress at different measuring temperatures, as shown in Fig. 8c. It is observed that the piezoelectric coefficient of the highest doped sample is increased with increasing stress and temperature and changed from 20.2 pC/N at $T=313$ K to 34.2 pC/N at $T=353$ K at stress of 6.27×10^5 Pa.

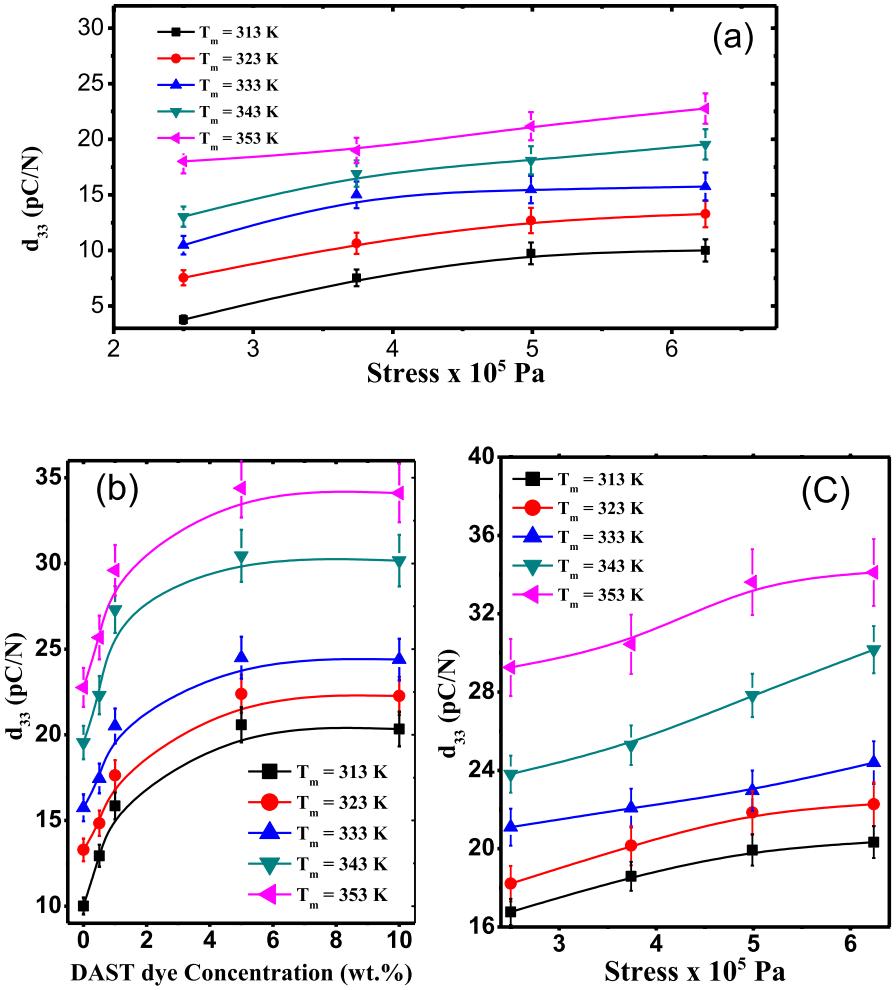

Fig. 9 d_{33} versus the stress at various temperatures for **a** pure P(VDF-HFP), **b** d_{33} variation versus DAST content at various temperatures and constant stress (6.24×10^5 Pa) and **c** d_{33} versus the stress at various temperatures for P(VDF-HFP)/10 wt% DAST. All the samples are poled with $E_p = 1.2\times10^7$ V/m at $T_p = 363$ K for $t_p = 30$ min

Conclusion

XRD results revealed that the characteristic peaks of α-phase almost disappear with increasing DAST dye concentration to the copolymer matrix, while the peaks related to the polar β-phase are improved. The analysis of FTIR showed that the relative β-phase fraction has been enhanced and became ~ 93.1% for P(VDF-HFP)/10 wt% of DAST dye. This enhancement of the polar phase of β is related to the interfacial electrostatic interaction between the atoms of fluorine that highly electronegative of P(VDF-HFP) copolymer and the positively charged DAST dye. The analysis of

UV–Vis results showed that the value of E_g for pure P(VDF-HFP) is 5.41 eV. As DAST dye is introduced into P(VDF-HFP), E_g decreased and became 3.75 eV for P(VDF-HFP)/10 wt% DAST. This reduction in the values optical band gap is attributed to the ability of the DAST dye to enhance charge transfer between the DAST and P(VDF-HFP) matrix. The pyroelectricity and piezoelectricity activities of the P(VDF-HFP)/DAST composites were found to be significantly higher than the pure P(VDF-HFP) copolymer. The piezoelectricity measurements display that the piezoelectric coefficient of pure P(VDF-HFP) and composite samples is enhanced with higher stress and measuring temperature and changed from ~ 3 pC/N at $T = 313$ K for pure P(VDF-HFP) to ~ 34 pC/N at $T = 353$ K for P(VDF-HFP)/ 10 wt% DAST composite sample. The improvement in the pyroelectricity and piezoelectricity is well correlated with the enhancement of electroactive β-phase of the composite samples. The optical, pyroelectricity and piezoelectricity of P(VDF-HFP) copolymer matrix were enhanced after introducing of DAST dye. This obviously contributes positively to the technology for fabricating a new generation of optoelectronic, transducers and energy storage devices.

Funding Open access funding provided by The Science, Technology & Innovation Funding Authority (STDF) in cooperation with The Egyptian Knowledge Bank (EKB).

Data availability All data generated or analyzed during this study are included in this submitted article. The authors declare that they do not use any custom code to generate or process the data described in the manuscript and any other information can be requested from the corresponding author.

Declarations

Conflict of interest The authors state there is no conflict of interest. It should be stated clearly before Acknowledgements.

References

1. Cai J, Hu N, Wu L, Liu Y, Li Y, Ning H, Liu X, Lin L (2019) Preparing carbon black/graphene/PVDF-HFP hybrid composite films of high piezoelectricity for energy harvesting technology. Compos Part A: Appl Sci Manuf 121:223–231. https://doi.org/10.1016/j.compositesa.2019.03.031
2. Abolhasani MM, Shirvanimoghaddam K, Naebe M (2017) PVDF/graphene composite nanofibers with enhanced piezoelectric performance for development of robust nanogenerators. Compos Sci Techn 138:49–56. https://doi.org/10.1016/j.compscitech.2016.11.017
3. Patil AH, Khanam BR, Dani S et al (2023) Enhancement in energy loss of relativistic electrons in ferroelectric PVDF above phase transition. Polym Bull 80:6851–6867. https://doi.org/10.1007/s00289-022-04399-5

4. Roy S, Thakur P, Hoque NA, Bagchi B, Das S (2016) Enhanced electroactive β-phase nucleation and dielectric properties of PVdF-HFP thin films influenced by montmorillonite and $Ni(OH)_2$ nanoparticle modified montmorillonite. RSC adv 6:21881–21894. https://doi.org/10.1039/C6RA00864J
5. Wu L, Yuan W, Hu N, Wang Z, Chen C, Qiu J, Ying J, Li Y (2014) Improved piezoelectricity of PVDF-HFP/carbon black composite films. J Phys D Appl Phys 47:135302. https://doi.org/10.1088/0022-3727/47/13/135302
6. Martins P, Lopes A, Lanceros-Mendez S (2014) Electroactive phases of poly (vinylidene fluoride): determination, processing and applications. Prog Polym Sci 39:683–706. https://doi.org/10.1016/j.progpolymsci.2013.07.006
7. Kim GH, Hong SM, Seo Y (2009) Piezoelectric properties of poly (vinylidene fluoride) and carbon nanotube blends: β-phase development. Phys Chem Chem Phys 11:10506–10512. https://doi.org/10.1039/B912801H
8. Doll W, Lando J (1970) The polymorphism of poly (vinylidene fluoride) IV. The structure of high-pressure-crystallized poly (vinylidene fluoride). J Macro Sci Part B 4:889–896. https://doi.org/10.1080/00222347008217130
9. Cui Z, Hassankiadeh NT, Zhuang Y, Drioli E, Lee YM (2015) Crystalline polymorphism in poly (vinylidenefluoride) membranes. Prog Polym Sci 51:94–126. https://doi.org/10.1016/j.progpolymsci.2015.07.007
10. Kumar M, Kumari P (2023) P(VDF-TrFE)/ZnO nanocomposite synthesized by electrospinning: effect of ZnO nanofiller on physical, mechanical, thermal, rheological and piezoelectric properties. Polym Bull 80:4859–4878. https://doi.org/10.1007/s00289-022-04275-2
11. Benz M, Euler WB (2003) Determination of the crystalline phases of poly (vinylidene fluoride) under different preparation conditions using differential scanning calorimetry and infrared spectroscopy. J Appl Polym Sci 89:1093–1100. https://doi.org/10.1002/app.12267
12. Lei D, Hu N, Wu L, Huang R, Lee A, Jin Z, Wang Y (2022) Preparation of efficient piezoelectric PVDF–HFP/Ni composite films by high electric field poling. Nanotechnol Rev 11:452–462
13. Zheng M-L, Fujita K, Chen W-Q, Duan X-M, Kawata S (2011) Two-photon excited fluorescence and second-harmonic generation of the DAST organic nanocrystals. J Phys Chem C 115:8988–8993. https://doi.org/10.1515/ntrev-2022-0025
14. Mongin O, Krishna TR, Werts MH, Caminade A-M, Majoral J-P, Blanchard-Desce M (2006) A modular approach to two-photon absorbing organic nanodots: brilliant dendrimers as an alternative to semiconductor quantum dots? Chem commun. https://doi.org/10.1039/B517270E
15. Xu X, Huang L, Fan K, Jiang Y, Sun Z, He Q, Ao T, Huang R, Wen Y, Ma C (2014) Electrical and optical properties of 4-N, N-dimethylamino-4′-N′-methyl-stilbazolium tosylate (DAST) modified by carbon nanotubes. J Mater Chem C 2:2394–2403. https://doi.org/10.1039/C3TC32209B
16. Bencivenni G, Saraiva Rosa N, Grieco P, Gillick-Healy MW, Kelly BG, Twamley B, Adamo MF (2022) Quaternary ammonium salts interact with enolates and sulfonates via formation of multiple+ NCH Hydrogen bonding interactions. Catalysts 12:803. https://doi.org/10.3390/catal12070803
17. Nishio M (2011) The CH/π hydrogen bond in chemistry. Conformation, supramolecules, optical resolution and interactions involving carbohydrates. Phys Chem Chem Phys 13:13873–13900. https://doi.org/10.1039/C1CP20404A
18. Ren L, Ping M, Zhang X (2020) Membrane biofouling control by surface modification of quaternary ammonium compound using atom-transfer radical-polymerization method with silica nanoparticle as interlayer. Membranes 10:417. https://doi.org/10.3390/membranes10120417
19. Cai X, Huang X, Zheng Z, Xu J, Tang X, Lei T (2017) Effect of polyaniline (emeraldine base) addition on α to β phase transformation in electrospun PVDF fibers. J Macro Sci, Part B 56:75–82. https://doi.org/10.1080/00222348.2016.1270730
20. Lei T, Cai X, Wang X, Yu L, Hu X, Zheng G, Lv W, Wang L, Wu D, Sun D (2013) Spectroscopic evidence for a high fraction of ferroelectric phase induced in electrospun polyvinylidene fluoride fibers. RSC Adv 3:24952–24958. https://doi.org/10.1039/C3RA42622J
21. Pratihar S, Patra A, Sasmal A, Medda SK, Sen S (2021) Enhanced dielectric, ferroelectric, energy storage and mechanical energy harvesting performance of ZnO–PVDF composites induced by MWCNTs as an additive third phase. Soft Matt 17:8483–8495. https://doi.org/10.1039/D1SM00854D
22. Vinila V, Isac J (2022) Synthesis and structural studies of superconducting perovskite GdBa2Ca3Cu4O10.5+δ nanosystems. Design, fabrication characterization of multifunctional nanomaterials. Elsevier, pp 319–41. https://doi.org/10.1016/B978-0-12-820558-7.00022-4

23. Das S, Alagarasan D, Varadharajaperumal S, Ganesan R, Naik R (2022) Tuning the nonlinear susceptibility and linear parameters upon annealing Ag_{60-x} Se_{40} Te_x nanostructured films for nonlinear and photonic applications. Mater Adv 3:7640–7654. https://doi.org/10.1039/D2MA00646D
24. Sasmal A, Medda SK, Devi PS, Sen S (2020) Nano-ZnO decorated $ZnSnO_3$ as efficient fillers in PVDF matrixes: toward simultaneous enhancement of energy storage density and efficiency and improved energy harvesting activity. Nanoscale 12:20908–20921. https://doi.org/10.1039/D0NR02057E
25. Imai Y, Kimura Y, Niwano M (2012) Organic hydrogen gas sensor with palladium-coated β-phase poly (vinylidene fluoride) thin films. Appl Phys Lett 101:181907
26. Janakiraman S, Surendran A, Ghosh S, Anandhan S, Venimadhav A (2016) Electroactive poly (vinylidene fluoride) fluoride separator for sodium ion battery with high coulombic efficiency. Solid Stat Ion 292:130–135. https://doi.org/10.1063/1.4764064
27. Shanthi PM, Hanumantha PJ, Albuquerque T, Gattu B, Kumta PN (2018) Novel composite polymer electrolytes of PVdF-HFP derived by electrospinning with enhanced Li-ion conductivities for rechargeable lithium–sulfur batteries. ACS Appl Energ Mater 1:483–94. https://doi.org/10.1021/acsaem.7b00094
28. Ma Y, Tong W, Wang W, An Q, Zhang Y (2018) Montmorillonite/PVDF-HFP-based energy conversion and storage films with enhanced piezoelectric and dielectric properties. Compos Sci Technol 168:397–403. https://doi.org/10.1016/j.compscitech.2018.10.009
29. Gomes J, Nunes JS, Sencadas V, Lanceros-Méndez S (2010) Influence of the β-phase content and degree of crystallinity on the piezo-and ferroelectric properties of poly (vinylidene fluoride). Smart Mater Struct 19:065010. https://doi.org/10.1088/0964-1726/19/6/065010
30. Ponnamma D, Erturk A, Parangusan H, Deshmukh K, Ahamed MB, Al Ali Al-Maadeed M (2018) Stretchable quaternary phasic PVDF-HFP nanocomposite films containing graphene-titania-$SrTiO_3$ for mechanical energy harvesting. Emerg Mater 1:55–65. https://doi.org/10.1007/s42247-018-0007-z
31. Vijayakumar T, Hubert Joe I, Reghunadhan Nair C, Jazbinsek M, Jayakumar V (2009) Electron–phonon coupling and vibrational modes contributing to linear electro-optic effect of the efficient NLO chromophore 4-(N, N-dimethylamino)-N-methyl-4′-toluene sulfonate (DAST) from their vibrational spectra. J Raman Spectrosc: Int J Orig Work Asp Raman Spectrosc Incl High Order Process Brillouin Rayleigh Scatt 40:52–63. https://doi.org/10.1002/jrs.2073
32. Li L, Zhang M, Rong M, Ruan W (2014) Studies on the transformation process of PVDF from α to β phase by stretching. Rsc Adv 4:3938–3943. https://doi.org/10.1039/C3RA45134H
33. Mandal D, Kim KJ, Lee JS (2012) Simple synthesis of palladium nanoparticles, β-phase formation, and the control of chain and dipole orientations in palladium-doped poly (vinylidene fluoride) thin films. Langmuir 28:10310–10317. https://doi.org/10.1021/la300983x
34. Sultana A, Sadhukhan P, Alam MM, Das S, Middya TR, Mandal D (2018) Organo-lead halide perovskite induced electroactive β-phase in porous PVDF films: an excellent material for photoactive piezoelectric energy harvester and photodetector. ACS Appl Mater Inter 10:4121–4130. https://doi.org/10.1021/acsami.7b17408
35. Crawford FS (1968) Waves, Berkeley physics course. https://cir.nii.ac.jp/crid/1574231873874657536
36. Sivakumar M, Subadevi R, Rajendran S, Wu H-C, Wu N-L (2007) Compositional effect of PVdF–PEMA blend gel polymer electrolytes for lithium polymer batteries. Euro Poly J 43:4466–4473. https://doi.org/10.1016/j.eurpolymj.2007.08.001
37. Mishra R, Singh SK, Gupta H, Tiwari RK, Meghnani D, Patel A, Tiwari A, Tiwari VK, Singh RK (2021) Polar β-Phase PVdF-HFP-Based freestanding and flexible gel polymer electrolyte for better cycling stability in a Na battery. Energy Fuels 35:15153–15165. https://doi.org/10.1021/acs.energyfuels.1c02114
38. Habib A, Metwally M, Fahmy T, Sarhan A (2022) Enhancement of optical and piezoelectric properties of P (Vinylidene fluoride-hexafluoropropylene)/N, N-Dimethyl-4-nitro-4-Stilbenamine composites for optoelectronic applications. Polym-Plast Techn Mater 61:2001–2015. https://doi.org/10.1080/25740881.2022.2086817
39. Raghu S, Archana K, Sharanappa C, Ganesh S, Devendrappa H (2015) The physical and chemical properties of gamma ray irradiated polymer electrolyte films. J Non-Cryst Solid 426:55–62. https://doi.org/10.1016/j.jnoncrysol.2015.06.018

40. Oikawa H, Fujita S, Kasai H, Okada S, Tripathy SK, Nakanishi H (2000) Electric field-induced orientation of organic microcrystals with large dipole moment in dispersion liquid. Colloids Surf A 169:251–258. https://doi.org/10.1016/S0927-7757(00)00467-2
41. Mott NF, Davis EA (2012) Electronic processes in non-crystalline materials. Oxford University Press
42. Soliman T, Vshivkov S (2019) Effect of Fe nanoparticles on the structure and optical properties of polyvinyl alcohol nanocomposite films. J Non-Cryst Solid 519:119452. https://doi.org/10.1016/j.jnoncrysol.2019.05.028
43. Ahmed M, Sarhan A, Elqahtani Z, Elsharkawy WB, Azzam M, Fahmy T (2022) Linear and non-linear optical parameters of copper chloride doped poly (vinyl alcohol) for optoelectronic applications. Egy J Chem 65(9):99–108. https://doi.org/10.21608/EJCHEM.2022.105927.4878
44. Elmahdy MM, Ahmed M, Aldhafeeri KA, Azzam MA, Fahmy T (2022) Thermal degradation and optical characteristics of plasticized poly (vinyl chloride-co-vinyl acetate-co-2-hydroxypropyl acrylate) terpolymer. J Mater Sci Mater Electr 33:23639–23658. https://doi.org/10.1007/s10854-022-09124-6
45. Atisme TB, Yu C-Y, Tseng EN, Chen Y-C, Hsu P-K, Chen S-Y (2019) Interface interactions in conjugated polymer composite with metal oxide nanoparticles. Nanomaterials 9:1534. https://doi.org/10.3390/nano9111534
46. Oriaku C, Osuwa J, Njoku C (2011) Single oscillator parameters and optical energies of laser irradiated Cu doped cds thin films. Non-Oxide Glas 3:25–30
47. Wemple S, DiDomenico M Jr (1971) Behavior of the electronic dielectric constant in covalent and ionic materials. Phys Rev B 3:1338. https://doi.org/10.1103/PhysRevB.3.1338
48. Fahmy T, Sarhan A (2021) Characterization and molecular dynamic studies of chitosan–iron complexes. Bull Mater Sci 44:1–12. https://doi.org/10.1007/s12034-021-02434-1
49. Ticha H, Tichy L (2002) Semiempirical relation between non-linear susceptibility (refractive index), linear refractive index and optical gap and its application to amorphous chalcogenides. J Optoelectron Adv Mater 4:381–386
50. Migahed M, Ishra M, El-Khodary A, Fahmy T (1993) Compatibility of polyacrylonitrile-butadiene with polyvinylchloride as explored by thermally stimulated depolarization current. Polym Test 12:335–349. https://doi.org/10.1016/0142-9418(93)90039-R
51. Migahed M, Ishra M, El-Khodary A, Fahmy T (1994) TSDC and the role of space charge in polyacrylonitrile/methylacrylate copolymer films. J Appl Polym Sci 53:1315–1322. https://doi.org/10.1002/app.1994.070531005
52. Migahed M, Fahmy T (1994) Structural relaxation around the glass transition temperature in amorphous polymer blends: temperature and composition dependence. Polymer 35:1688–1693. https://doi.org/10.1016/0032-3861(94)90843-5
53. Fahmy T, Hafiz H, Ahmed M (2002) Structural and relaxation aspects in azodye-doped abs films: TSDC study. Inter J Polym Mater Polym Biomater 51:875–889. https://doi.org/10.1080/714975671
54. Ahmed M, Fahmy T (2011) Study of the relaxation phenomenon of Poly (vinyl chloride-co-vinylacetate-co-2-hydroxypropyl acrylate)/Poly (methyl methacrylate) blends using TSDC-TS technique: dipole-dipole interaction approach. J Korean Phys Soci 59:98–104. https://doi.org/10.3938/jkps.59.98
55. Elhadidy H, Abdelhamid M, Aboelwafa A, Habib A (2013) Structure and piezoelectricity of poly (styrene-co-acrylonitrile) copolymer doped with different dyes. Polym-Plast Technol Eng 52:1277–1284. https://doi.org/10.1080/03602559.2013.814676
56. Elsharkawy WB, Elqahtani ZM, Fahmy T (2021) Rate theory and relaxation map analysis of iodine-doped poly (Ethyl Methacrylate) composite films using thermally stimulated depolarization current-thermal sampling (TSDC-TS) technique. Egy J Chem 64(10):5457–70. https://doi.org/10.21608/EJCHEM.2021.69217.3516
57. Garg M, Quamara J (2006) Multiple relaxation processes in high-energy ion irradiated kapton-H polyimide: thermally stimulated depolarization current study. Nucl Instrum Methods Phys Res Sect B 246:355–363. https://doi.org/10.1016/j.nimb.2006.01.012
58. Saxena P, Gaur M, Khare P (2009) Effect of blending with polysulfone on thermally stimulated discharge behavior of polyvinylidenefluoride films. Polym-Plast Technol Engin 48:415–422. https://doi.org/10.1080/03602550902725415
59. Sagar R, Gaur M, Bhadoria B (2018) Investigation of TSDC and dielectric modulus of PVDF–$BaZrO_3$ nanocomposites thin film. Vacuum 156:375–383. https://doi.org/10.1016/j.vacuum.2018.07.037

60. Bucci C, Fieschi R, Guidi G (1966) Ionic thermocurrents in dielectrics. Phys Rev 148:816. https://doi.org/10.1103/PhysRev.148.816
61. Hino T, Suzuki K (1973) Method for measuring distribution of relaxation time of dipoles by thermally stimulated current. Elect Eng Japan 93:31–36. https://doi.org/10.1002/eej.4390930506
62. Garlick G, Gibson A (1948) The electron trap mechanism of luminescence in sulphide and silicate phosphors. Proc Phys Soc 60:574. https://doi.org/10.1088/0959-5309/60/6/308
63. Kakutani H (1970) Dielectric absorption in oriented poly (vinylidene fluoride). J Polym Sci Part A Polym Phys 8(7):1177–1186. https://doi.org/10.1002/pol.1970.160080712
64. Malmonge LF, Malmonge JA, Sakamoto WK (2003) Study of pyroelectric activity of PZT/PVDF-HFP composite. Mater Res 6:469–473. https://doi.org/10.1590/S1516-14392003000400007
65. Abdelhamid M, Aboelwafa A, Elhadidy H, Habib A (2012) Investigation of the structure and piezoelectricity of poly (vinylidene fluoride–trifluroethylene) copolymer doped with different dyes. Inter J Polym Mater 61:505–519. https://doi.org/10.1080/00914037.2011.593063
66. Satish B, Sridevi K, Vijaya M (2002) Study of piezoelectric and dielectric properties of ferroelectric PZT-polymer composites prepared by hot-press technique. J Phys D Appl Phys 35:2048. https://doi.org/10.1088/0022-3727/35/16/321
67. Kuo W-K, Shieh M-Y, Yu H-H (2011) Three-dimensional infrared absorption of hot-drawn and poled electro-optic PVDF films. Mater Chem Phys 129:130–133. https://doi.org/10.1016/j.matchemphys.2011.03.074
68. Saxena P, Shukla P (2022) A comparative analysis of the basic properties and applications of poly (vinylidene fluoride) (PVDF) and poly (methyl methacrylate) (PMMA). Polym Bull 79:5635–5665. https://doi.org/10.1007/s00289-021-03790-y

Authors and Affiliations

A. Habib[1] · M. M. Metwally[2] · T. Fahmy[1]

✉ A. Habib
ahmedhabib@mans.edu.eg

[1] Polymer Research Group, Physics Department, Faculty of Science, Mansoura University, Mansoura ET-35516, Egypt

[2] Chemistry Department, Faculty of Science, Mansoura University, Mansoura ET-35516, Egypt